International Journal of Environmental Science and Technology
https://doi.org/10.1007/s13762-020-03103-2

ORIGINAL PAPER

Adsorption potentials of iron-based metal–organic framework for methyl orange removal: batch and fixed-bed column studies

A. Karami[1] · R. Sabouni[1] · M. H. Al-Sayah[2] · A. Aidan[1]

Received: 6 June 2020 / Revised: 19 November 2020 / Accepted: 21 December 2020

Abstract

In the present work, continuous fixed-bed column and batch studies were undertaken to investigate the efficiency of iron-based metal–organic framework (Fe-BTC) for the removal of methyl orange as a model contaminant from aqueous solutions. The batch experiments were carried out by varying operational parameters such as adsorbent dosage, pH, temperature, and initial contaminant concentration. The results showed that Fe-BTC had a high removal efficiency under a wide pH range. The equilibrium data were best fitted by the Langmuir model with a maximum adsorption capacity of 100.3 mg g^{-1} at 298 K. In order to assess the industrial feasibility of Fe-BTC, fixed-bed column studies were conducted to obtain breakthrough curves, breakthrough and saturation times, and maximum uptakes at different bed heights. The breakthrough time was 20.0 and 46.2 h at 0.75 and 1.5 cm bed depths, respectively. The bed removal efficiency was 35.2 and 46.7% at 0.75 and 1.5 cm bed depth, respectively. The bed maximum adsorption capacity was 20.2 and 21.6 mg/g at 0.75 and 1.5 cm bed depths, respectively. Moreover, the application of empirical breakthrough curve models showed good agreement with the modified dose response model ($R^2 > 0.99$). Also, the analytical solution of the advection–dispersion–adsorption mass transfer equation showed an excellent fit to the experimental breakthrough data ($R^2 > 0.99$). Further, the analytical model was utilized to predict the length of the mass transfer zone as a function of the bed depth and to construct a 3D surface plot that can be utilized to predict the breakthrough at different bed depths.

Graphic Abstract

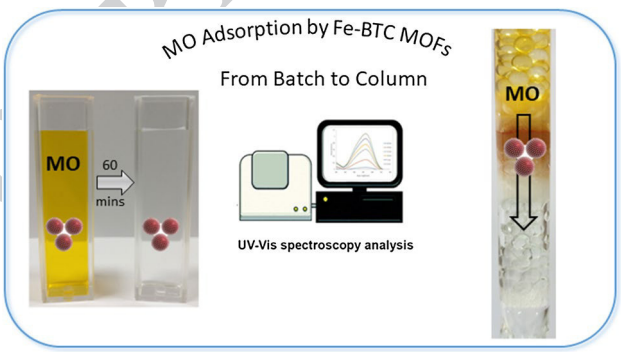

Keywords Breakthrough curve · Fe-BTC · Fixed-bed column · Langmuir isotherm · Metal–organic frameworks · Methyl orange

Editorial responsibility: Samareh Mirkia.

Supplementary Information The online version contains supplementary material available at https://doi.org/10.1007/s13762-020-03103-2.

Extended author information available on the last page of the article

Introduction

Over the last few decades, adsorption has gained tremendous attention as an efficient industrial process in separation, wastewater treatment, and purification. Adsorption can

be used to separate, decolorize and deodorize contaminants from liquid solution and gas mixtures. In the field of water purification, water contamination by pollutants such as pharmaceuticals, pesticides, detergents, endocrine-disrupting chemicals, and organic dyes is at the center of tremendous scientific research efforts due to their potential risks to both human and aquatic environment (Arslan et al. 2017). In particular, dyes contain toxic compounds that are resistant to biodegradation and photodegradation, thus cannot be removed with conventional wastewater treatment technologies. Consequently, these contaminants may end up in the aquatic environment, becoming threats to wildlife and may eventually end up in the groundwater or drinking water (Luo et al. 2014). Accordingly, dye removal is crucial for both environmental and quality aspects.

Among water purification methods, adsorption is often viewed favorably since it offers a cost-effective, simple, and flexible process for water purification (Yagub et al. 2014; Karami et al. 2020). Furthermore, the adsorption process generally does not produce harmful by-products (Liu et al. 2019). The adsorption process has been widely used, not only for dyes removal, but also has been applied for the removal of various classes of chemical contaminants produced from industrial effluents that are practically persistent to conventional treatment methods, such as heavy metals and various organic pollutants (Yagub et al. 2014; Wu et al. 2018). Adsorption can be performed either in a batch or a continuous setup. The batch adsorption process is not a favorable choice for large-scale industrial applications because it is restricted to small wastewater volumes with minimal pollution load. Batch adsorption studies are usually limited to determining the adsorbent's removal efficiency toward a particular pollutant and understanding the possible adsorption mechanism (Dichiara et al. 2015). The column adsorption process, on the other hand, is more appropriate for industrial settings as it allows for the processing of large volumes of wastewater. When performing adsorption in a fixed-bed column setup, complete removal of the pollutant from the water can be accomplished until a specific time (breakthrough), whereas this is not the case in the batch setup where at equilibrium, the contaminate residual concentration will not be zero (Dichiara et al. 2015). However, to properly design an adsorption column, a batch adsorption investigation is required to understand the nature of the adsorption process. In particular, various batch experiments are performed to determine both equilibrium and kinetics behavior of the adsorbate/adsorbent couple.

The design and the success of any adsorption process, however, pivots on the removal efficiency and the loading capacity of the adsorbent (Tan et al. 2019). Therefore, the choice of the adsorbent is a crucial aspect of the process. Among the potential candidates are metal–organic frameworks (MOFs), which are porous solids formed of organic–inorganic networks that are built by metal ions coordinated with organic ligands (Tan et al. 2019). MOFs have impressive adsorbent characteristics like high internal surface area (Farha et al. 2012; Furukawa et al. 2013), high thermal stability (Furukawa et al. 2011), tunable pore volumes/shapes (Farha et al. 2012; Furukawa et al. 2013), and flexible crystal structures (Aguilera-Sigalat and Bradshaw 2016). These exceptional properties have led to numerous studies that investigate the removal of several pollutants from contaminated water using MOFs as adsorbents in batch adsorption setups (Adeyemo et al. 2012; Khan et al. 2013; Dias and Petit 2015; Hasan and Jhung 2015; Ayati et al. 2016; Liu et al. 2017; Samokhvalov 2018; Dhaka et al. 2019; Joseph et al. 2019). The results have shown that MOFs are robust adsorbents with excellent removal efficiencies, high loading capacities, and tunable selectivity. However, most of the reported studies were conducted and in batch setups, and very few studies have explored the potential application of MOFs in fix-bed column adsorption processes (He et al. 2019; Arora et al. 2019; Zhang et al. 2020).

Therefore, this study was set to construct a fixed-bed column and investigate the adsorption process of a model pollutant (methyl orange (MO)) from contaminated water using MOF-based adsorbent, iron 1,3,5-benzenetricarboxylate (Fe-BTC). Fe-BTC is an iron-based MOF and was reported for the removal of various compounds from liquids (Centrone et al. 2011; Zhu et al. 2012) in batch setups, and only one study reported a limited investigation on its use for the removal of Pb(II) and Cd(II) from aqueous solutions in fixed-bed column (Zhang et al. 2020). This MOF was selected in this study due to the limited number of studies on its adsorption efficiency for dyes in fixed-bed column. Furthermore, Fe-BTC is commercially available, which makes it preferable to other MOFs in environmental applications and has shown good water stability (Zhu et al. 2012; Dhakshinamoorthy et al. 2012). Besides, iron-based MOFs in general (including Fe-BTC) are gaining interest in the field of environmental remediation because of the abundant availability of iron as a raw material and because they displayed high thermal and mechanical stability, which helps in avoiding the aggregation problem that other nanomaterials suffer from (Zhu et al. 2012; Liu et al. 2017). Methyl orange, on the other hand, has been chosen as an adsorbate model molecule because it is used as a colorant in various industrial applications (Mittal et al. 2007). To the best of the authors' knowledge, this research work is one of the few studies (He et al. 2019; Arora et al. 2019; Zhang et al. 2020) that deploys MOFs in a continuous fixed-bed adsorption column.

The investigation was designed to have a complete picture of the kinetics and the thermodynamics for the removal of MO using Fe-BTC in batch and fixed-bed column settings. In the first part of the study, the adsorption kinetics and isotherms were analyzed, and the thermodynamic parameters

Journal : Large 13762 | Article No : 3103 | Pages : 16 | MS Code : 3103 | Dispatch : 28-12-2020

were calculated from batch adsorption experiments. The second part consists of building a bench-scale fixed-bed column, packed with Fe-BTC for MO removal from water in a continuous setup, and recording the breakthrough performance at different bed depths. Additionally, empirical breakthrough models, including Thomas, Yoon-Nelson, Clark, and the modified dose response (MDR), have been used to analyze the breakthrough curve. The analytical solution of the advection–dispersion–adsorption mass transfer model was also applied to predict the adsorption breakthrough curve and the mass transfer zone. The parameters related to each model, along with the regression coefficients, were calculated. The aforementioned studies were conducted in 2019 at the American University of Sharjah.

Materials and methods

Materials

Fe-BTC was obtained from Sigma-Aldrich (Basolite® F300) and was used without further modifications. The MO stock solution (1000 mg/L) was purchased from LabChem (USA), and the desired MO aqueous solutions were made by dilution using deionized water (PURELAB® Pulse, ELGA LabWater, UK). Aqueous solutions of HCl and NaOH (1 M) were used for pH adjustment. Finally, ethanol (99.8%, Sigma-Aldrich) was used as for Fe-BTC regeneration.

Characterization

Fe-BTC samples were characterized before and after the adsorption experiments. The crystal structure of the samples was verified using X-ray diffraction (XRD) measurements. In this work, XRD patterns of the samples were collected using Bruker D8 ADVANCE diffractometer (Cu-Kα radiation with $\lambda = 1.5406$ Å). The 2θ range was 5.0°–60°, and the step size was 0.03°. The shape and morphology of the samples were inspected using a transmission electron microscope (TEM). Fourier transform infrared (FTIR) spectra were obtained on the FTIR spectrophotometer (PerkinElmer, USA) using the KBr disk method, in the range of 4000–450 cm^{-1}, and 10 scans were signal-averaged with a resolution of 1.0 cm^{-1}. Thermal gravimetric analysis (TGA) of Fe-BTC samples were measured using a Pyris 1 TGA instrument (PerkinElmer, USA) at a heating rate of 10 °C min^{-1} from 30 to 700 °C. The surface point zero charge (pH_{PZC}) of Fe-BTC was determined using the solid addition method (Fiol and Villaescusa 2009; Hosseini et al. 2011). The characterization results, including XRD, FTIR, TEM, and TGA, are presented in the supplementary information.

Adsorption experiments

Batch adsorption

Each batch experiment was carried out by adding a measured amount of adsorbent to 50 mL MO solution with initial concentration at a specific pH and temperature. The solid and liquid were stirred vigorously and maintained for a predetermined time of (5 min to 3 h) to ensure complete adsorption. The samples were taken using 5 mL syringe and filtered using membrane filters (Nylon, 17 mm diameter, 0.45 µm pore size). Then, the concentration of MO was determined by measuring the absorbance ($\lambda = 464$ nm) of the solutions with a UV–Vis spectrophotometer (Evolution 60s, USA). The adsorbed amount of MO at any time (q_t) was calculated by Eq. (1).

$$q_t = \frac{(C_o - C_t) \times V}{m} \tag{1}$$

where q_t is the MO adsorption capacity (mg/g), C_o is the MO initial concentration in the aqueous solution (mg/L), C_t is the MO residual concentrations in the solution at time t (min), V is the total volume of the solution in the beaker (L), and m is the adsorbent's dosage (mg). The removal efficiency of MO can also be found from Eq. (2).

$$\mathrm{RE} = \frac{C_o - C_t}{C_o} \times 100 \tag{2}$$

Furthermore, to ensure that no MO degradation is taking place, a control experiment was performed.

Adsorption kinetics Kinetic experiments were performed at initial concentrations in the range 5–15 mg/L. The kinetic data obtained were analyzed using pseudo-first-order (PFO) (Tan and Hameed 2017), pseudo-second-order (PSO) (Tan and Hameed 2017), and Elovich (Tan and Hameed 2017) models. Also, the intraparticle diffusion (IPD) kinetics were examined using the model developed by Weber and Morris (Weber and Morris 1963). The PFO, PSO, and Elovich kinetic models are given in Eqs. (3), (4) and (5), respectively.

$$q_t = q_e\left(1 - e^{-k_1 t}\right) \tag{3}$$

$$q_t = \frac{k_2 q_e^2 t}{1 + k_2 q_e t} \tag{4}$$

$$q_t = \frac{1}{\beta} \ln(1 + \alpha\beta t) \tag{5}$$

where k_1 (min^{-1}) represents the PFO kinetic constant, k_2 (g mg^{-1} min^{-1}) is the PSO kinetic constant, α (mg g^{-1} min^{-1}) is the initial adsorption rate and β (g mg^{-1}) is the desorption constant linked to the surface coverage extent and the activation energy (Ghaedi et al. 2014). All kinetic parameters were determined using a nonlinear regression technique.

Also, the Weber–Morris intraparticle diffusion (IPD) model is expressed in Eq. (6),

$$q_t = k_P t^{0.5} + C \tag{6}$$

where k_P (mg g^{-1} $min^{-0.5}$) is the IPD rate constant, and C (mg g^{-1}) is the IPD constant linked to the boundary layer thickness (Weber and Morris 1963).

Adsorption isotherms The MO equilibrium adsorption isotherms were studied with initial concentration ranges of 10–250 mg/L and Fe-BTC dosage of 50 mg. The obtained adsorption equilibrium data were fitted to Langmuir (Langmuir 1918), Freundlich (Liu and Liu 2008), Dubinin–Radushkevich (D–R) (Liu and Liu 2008), and Temkin (Liu and Liu 2008) isotherm models. The Langmuir isotherm is given by Eq. (7)

$$q_e = \frac{q_m K_L C_e}{1 + K_L C_e} \tag{7}$$

where q_m is the maximum monolayer adsorption capacity (mg g^{-1}), K_L is the Langmuir constant (L mg^{-1}). From the value of K_L, the Langmuir dimensionless separation factor or equilibrium parameter (R_L) is calculated by Eq. (8).

$$R_L = \frac{1}{\left(1 + K_L C_o\right)} \tag{8}$$

where R_L indicates the shape of the isotherm to be either irreversible ($R_L = 0$), favorable ($0 < R_L < 1$), linear ($R_L = 1$), or unfavorable ($R_L > 1$) (Baccar et al. 2010).

The Freundlich isotherm is expressed in Eq. (9).

$$q_e = K_F C_e^{1/n} \tag{9}$$

where n and K_f ((mg g^{-1})(L mg^{-1})$^{1/n}$) are Freundlich constants linked to the adsorption favorability and capacity, respectively. If $(1/n) < 1$, it indicates favorable adsorption (Baccar et al. 2010).

The Temkin isotherm is given in Eq. (10).

$$q_e = \frac{RT}{b_T} \ln\left(K_T C_e\right) \tag{10}$$

where K_T (L mg^{-1}) is the Temkin isotherm constant, and b_T (kJ mol^{-1}) is the constant related to the heat of adsorption. R is the universal gas constant, and T (K) is the absolute temperature.

Finally, Eqs. (11) and (12) present the D–R isotherm model.

$$q_e = q_{DR} e^{-K_{DR}\phi^2} \tag{11}$$

$$\phi = RT \ln\left(1 + \frac{1}{C_e}\right) \tag{12}$$

where q_{DR} (mg g^{-1}) is the D–R constant representing the theoretical adsorption capacity, φ is the Polanyi potential, and K_{DR} (mol^2 kJ^{-2}) is the constant of the adsorption energy which can be correlated to the mean adsorption energy (E) by using Eq. (13).

$$E = \frac{1}{\sqrt{2K_{DR}}} \tag{13}$$

In general, the calculated value of E can be useful to determine whether the adsorption is physical or chemical. If the value of E is between 8 and 16 kJ mol^{-1}, then the adsorption is dominated by a chemical mechanism, while if $E < 8$ kJ mol^{-1}, then the adsorption proceeds through a physical mechanism (Vijayaraghavan et al. 2006; Basar 2006; Kousha et al. 2012).

Adsorption thermodynamics MO adsorption at 298, 303, and 313 K was investigated, and the thermodynamic parameters Gibbs free energy ($\Delta G°$), change in enthalpy ($\Delta H°$), and change in entropy ($\Delta S°$) were calculated. Equations (14) and (15) were utilized to determine $\Delta G°$, $\Delta H°$, and $\Delta S°$,

$$\Delta G° = -RT \ln\left(K_{eq}\right) \tag{14}$$

$$\ln\left(K_{eq}\right) = \frac{\Delta S°}{R} - \frac{\Delta H°}{RT} \tag{15}$$

where K_{eq} is the adsorption equilibrium constant. In order to obtain relevant values for the thermodynamic parameters, the value of K_{eq} has to be correctly estimated. The Langmuir constant (K_L) was used to estimate K_{eq} using the method suggested by Zhou and Zhou (2014).

Fixed-bed column adsorption

A schematic representation of the experimental setup is shown in Figure S11. The fixed-bed continuous adsorption experiments were conducted in a cylindrical glass column (10 mm inner diameter). The adsorption column was packed with 150 or 300 mg of Fe-BTC to achieve 0.75 or 1.5 cm bed depths, respectively. The bed was positioned between the top and bottom layers of deactivated glass wool (RESTEK, USA) and glass beads (4 mm diameter). The bottom layer provided support for the bed, while the top layer offers proper liquid distribution across the

Journal : Large 13762 | Article No : 3103 | Pages : 16 | MS Code : 3103 | Dispatch : 28-12-2020

column's cross-section. The MO solution of 15 mg/L influent concentration (C_o) was fed to the column, and to ensure a constant flow rate ($Q = 4.5$ mL/h), a constant level of the hydrostatic head above the fixed-bed was maintained. Then, the column's effluent was collected at different time intervals and were analyzed for MO concentration (C_t) using a UV–VIS spectrophotometer. The cumulative volume of the effluent was also recorded with each sample. The measured concentration data were normalized with respect to C_o and plotted against the operating time (t) and collected volume (V) to obtain the breakthrough curves (BTCs). Finally, to assess the performance of the column, the breakthrough (t_b) and the exhaustion times (t_e) were set as the time to achieve a normalized concentration (C_t/C_o) of 0.1 and 0.9, respectively.

Fixed-bed column performance equations In order to evaluate the operational performance and dynamic response of the fixed-bed column, it is important to determine the breakthrough time and the shape of the breakthrough curve.

From the experimental data of the breakthrough curve, the total amount of MO adsorbed at the exhaustion point (m_{ad}) was calculated using Eq. (16).

$$m_{ad} = QC_o \int_0^{t_e} \left(1 - \frac{C_t}{C_o}\right) dt \tag{16}$$

where Q is the inlet volumetric flow rate, C_o is the influent MO concentration, and C_t/C_o is the ratio of the effluent concentration to the influent concentration.

Also, the total amount of MO fed to the column at the exhaustion point (m_{tot}) is calculated using Eq. (17).

$$m_{tot} = QC_o t_e \tag{17}$$

From the values of m_{ad} and m_{tot}, the bed removal efficiency (RE_{bed}) is calculated as follows:

$$RE_{bed} = \frac{m_{ad}}{m_{tot}} \times 100 \tag{18}$$

Dividing the total amount of MO adsorbed at the exhaustion point (m_{ad}) by the adsorbent mass (m) gives the maximum adsorption capacity, also known as the equilibrium adsorption capacity (q_{max}) is calculated by Eq. (19).

$$q_{max} = \frac{m_{ad}}{m} \tag{19}$$

The empty bed contact time (EBCT) is the time during which the liquid feed is in contact with the adsorbent in the column, assuming that the liquid flows through the bed at the same velocity, is given by:

$$EBCT = \frac{Z \times A_{bed}}{Q} \tag{20}$$

where Z is the bed depth in the column, and A_{bed} is the cross-section area of the bed.

Finally, the length of the mass transfer zone (MTZ) in the bed is calculated by Eq. (21).

$$MTZ = Z \times \left(1 - \frac{t_b}{t_e}\right) \tag{21}$$

Empirical breakthrough models The prediction of the concentration–time profile and maximum adsorption capacity of an adsorbent are necessary factors for the successful design of the industrial adsorption column. Therefore, in this work, breakthrough data were analyzed using Thomas (1944), Yoon and Nelson (1984), (Clark 1987), and modified dose response (MDR) (Yan et al. 2001) models, which are given in Eqs. (22), (23), (24), and (25), respectively.

$$\frac{C_t}{C_o} = \frac{1}{1 + \exp\left[K_{TH}\left(\frac{q_{TH}m}{Q} - C_o t\right)\right]} \tag{22}$$

$$\frac{C_t}{C_o} = \frac{1}{1 + \exp\left[K_{YN}(\tau - t)\right]} \tag{23}$$

$$\frac{C_t}{C_o} = \left(\frac{1}{1 + Ae^{-rt}}\right)^{\frac{1}{n-1}} \tag{24}$$

$$\frac{C_t}{C_o} = 1 - \frac{1}{1 + \left(\frac{C_o Q t}{q_{MDR} m}\right)^{a_{MDR}}} \tag{25}$$

where K_{TH} is the Thomas rate constant, q_{TH} is the equilibrium (maximum) adsorption capacity predicted by the Thomas model, m is the MOF's mass in the column, C_o is the influent concentration, C_t is the effluent concentration, Q is the flow rate, and t is the sampling time. Also, K_{YN} is the Yoon–Nelson rate constant, and τ is the time required for a 50% adsorbate breakthrough. In Eq. (24), A and r are the Clark model constants, and n is the Freundlich isotherm constant. Finally, a_{MDR} is the MDR model constant, and q_{MDR} is the equilibrium (maximum) adsorption capacity predicted by the MDR model.

Analytical solution of the dynamic advection–dispersion–adsorption model In addition to the empirical models used to simulate the breakthrough curves, the one-dimensional dynamic advection–dispersion–adsorption model given in Eq. (26) was solved analytically to predict the breakthrough and MTZ of MO adsorption in the fixed-bed column.

$$\frac{\partial C}{\partial t} = D_L \frac{\partial^2 C}{\partial Z^2} - u\frac{\partial C}{\partial t} - \frac{\rho_b}{\varepsilon}\frac{\partial q}{\partial t} \quad (26)$$

where C and q are the MO concentration in the liquid and solid phases, respectively. The bed depth, longitudinal dispersion coefficient, fixed-bed bulk density, porosity, and interstitial velocity are indicated by Z, D_L, ρ_b, ε, and u, respectively. Finally, t is the operating time (independent variable). The interstitial velocity (u) can be calculated using Eq. (27).

$$u = \frac{4Q}{\pi\varepsilon d_{in}^2} \quad (27)$$

where d_{in} is the inside diameter of the column.

The model is developed on the assumption that the mass transfer in the column is governed by the advection–dispersion–adsorption mechanism without degradation (chemical reaction) (Zheng and Bennett 2002). The simplification of Eq. (26) was formulated as follows (Apiratikul 2020):

At low MO concentration in the influent, the relation between q and C can be assumed to be a linear one, as expressed in Eq. (28).

$$q = K_P C \quad (28)$$

where K_p is the linear adsorption coefficient. Substituting Eq. (28) in Eq. (26) and rearranging gives Eq. (29).

$$\left(1 + \frac{\rho_b}{\varepsilon}K_P\right)\frac{\partial C}{\partial t} = D_L\frac{\partial^2 C}{\partial Z^2} - u\frac{\partial C}{\partial t} \quad (29)$$

By defining the retardation coefficient, R_f, as in Eq. (30)

$$R_f = \left(1 + \frac{\rho_b}{\varepsilon}K_P\right) \quad (30)$$

and substituting in Eq. (29), followed by division of both sides by R_f yields

$$\frac{\partial C}{\partial t} = \frac{D_L}{R_f}\frac{\partial^2 C}{\partial Z^2} - \frac{u}{R_f}\frac{\partial C}{\partial t} \quad (31)$$

To further simplify Eq. (31), the terms $\frac{D_L}{R_f}$ and $\frac{u}{R_f}$ are defined as the effective longitudinal dispersion coefficient (D_{eff}) and effective velocity (u_{eff}), respectively, to give the final form of the partial differential equation to be solved.

$$\frac{\partial C}{\partial t} = D_{eff}\frac{\partial^2 C}{\partial Z^2} - u_{eff}\frac{\partial C}{\partial t} \quad (32)$$

The solution of Eq. (32) needs two boundary conditions and one initial condition as follows:

Boundary condition 1: $C|_{Z=0} = C_o; t \geq 0$

Boundary condition 2: $C|_{Z=\infty} = 0; t \geq 0$

Initial condition: $C|_{t=0} = 0; Z \geq 0$

The analytical solution of Eq. (32) with the stated boundary and initial conditions was first proposed by Ogata and Banks (1961) and is given in Eq. (33).

$$\frac{C}{C_o} = \frac{1}{2}\left[\operatorname{erfc}\left(\frac{Z - u_{eff}t}{2\sqrt{D_{eff}t}}\right) + e^{\frac{u_{eff}Z}{D_{eff}}}\operatorname{erfc}\left(\frac{Z + u_{eff}t}{2\sqrt{D_{eff}t}}\right)\right] \quad (33)$$

where $\operatorname{erfc}(x)$ is the complementary error function in which x stands for the term in the parenthesis of the complementary error function in Eq. (33). The function is defined in Eq. (34) as follows:

$$\operatorname{erfc}(x) = 1 - \frac{2}{\sqrt{\pi}}\int_0^x e^{-\eta^2} d\eta \quad (34)$$

The values of the fixed-bed parameters (i.e., ρ_b, ε, u, and d_{in}) that are used in the modeling of the breakthrough curve are summarized in Table S4.

Error analysis

Three error functions are used to quantitatively assess the fitting accuracy of the employed kinetic and isotherm models, which are the coefficient of determination (R^2), root-mean-square error (RMSE), and the sum of squared errors (SSE). These functions are expressed in Eqs. (35–37).

$$R^2 = \frac{\sum_{i=1}^{N}\left(q_{e,i} - q_{e,avg}\right)^2 - \sum_{i=1}^{N}\left(q_{e,i} - q_{p,i}\right)^2}{\sum_{i=1}^{N}\left(q_{e,i} - q_{e,avg}\right)^2} \quad (35)$$

$$\text{RMSE} = \sqrt{\frac{1}{N}\sum_{i=1}^{N}\left(q_{p,i} - q_{e,i}\right)^2} \quad (36)$$

$$\text{SSE} = \sum_{i=1}^{N}\left(q_{p,i} - q_{e,i}\right)^2 \quad (37)$$

where q_e, q_p, and $q_{e,avg}$ are the experimental adsorbed amount of MO (mg/g), the predicted value from the isotherm model corresponding to C_e (mg/L), and the average of q_e, respectively. N denotes the number of experimental data points. The values of the error functions were calculated using the regression tool in MATLAB.

Journal : Large 13762 | Article No : 3103 | Pages : 16 | MS Code : 3103 | Dispatch : 28-12-2020

Results and discussion

Batch adsorption

Effect of contact time

The rate of adsorption and the loading capacity of the adsorbent are essential aspects of the adsorption process, which are dependent on the pollutant load of the contaminated water. Thus, the rate of adsorption of MO by Fe-BTC at different initial concentrations of MO was investigated. The results depicted in Figure S5 show that the adsorption process was very rapid, and most MO is adsorbed in the first 10 min and reaching equilibrium in ~ 1 h. This is attributed to the abundance of unoccupied active sites on the surface of the adsorbent. As time progressed, the adsorption rate gradually decreased due to a decrease in the available active sites and eventually reaching saturation (Haque et al. 2010).

Effect of initial pH (pH_i) and adsorption mechanism

The pH has a crucial effect on adsorption processes due to its impact on the charge of both the adsorbent and the adsorbate, which in turn affect the electrostatic interactions between the two. Thus, the effect of initial pH (pH_i) on the loading capacity of Fe-BTC in the range of pH 2–12 at 298 K have been investigated. The initial concentration of MO was fixed at 15 mg/L, and the dosage of Fe-BTC was 150 mg (50 mL total solution volume).

The results (Fig. 1a) show that there was an insignificant effect on Fe-BTC adsorption capacity of MO in the range of 2–10. This is attributed to the dominant positive charge on the surface of Fe-BTC, which enhances the electrostatic attraction between the MOF's surface and the negatively charged MO molecules (MO usually exists in the anionic form) (Haque et al. 2010; Wu et al. 2017). This was further supported by the zero-surface charge (PZC) experiment (See Fig. 1b), which indicates that the MOF is positively charged at a pH range lower than 10. However, as pH_i increases to 12, which is higher than pH_{PZC}, the adsorption capacity dropped significantly either because a strong repulsion between the surface of Fe-BTC and MO molecules which are both negatively charged (Haque et al. 2010; Wu et al. 2017) or due to the collapse of the structure of Fe-BTC under strongly basic conditions (Wu et al. 2017). Furthermore, the relatively constant adsorption capacity in the range 2–10 may imply the presence of π-π stacking interaction between benzene rings in the carboxylic group of Fe-BTC and MO molecules (Hasan and Jhung 2015). Similar behavior has been suggested for the liquid phase adsorption of other organic molecules over MOFs (Huo and Yan 2012; Park et al. 2013; Jia et al. 2015; Qin et al. 2015). Consequently, all subsequent experiments were carried out without adjusting the pH of the MO solution (pH = 6).

Effect of initial concentration and MOF dosage

The results in Figure S6 reveal the effect of initial MO concentration on the adsorption capacity. It can be seen that as the initial concentration increases, the adsorption capacity increases as well. As initial MO increased from 10 to 160 mg/L, the adsorption capacity of the dye on Fe-BTC increased from 6.74 to 65.1 mg/g. This can be attributed to the higher driving force for mass transfer from solution to the adsorbent as the initial dye concentration increases at a constant adsorbent dosage, and as a result, leads to an increase in MO uptake by the adsorbent (Abdi et al. 2017).

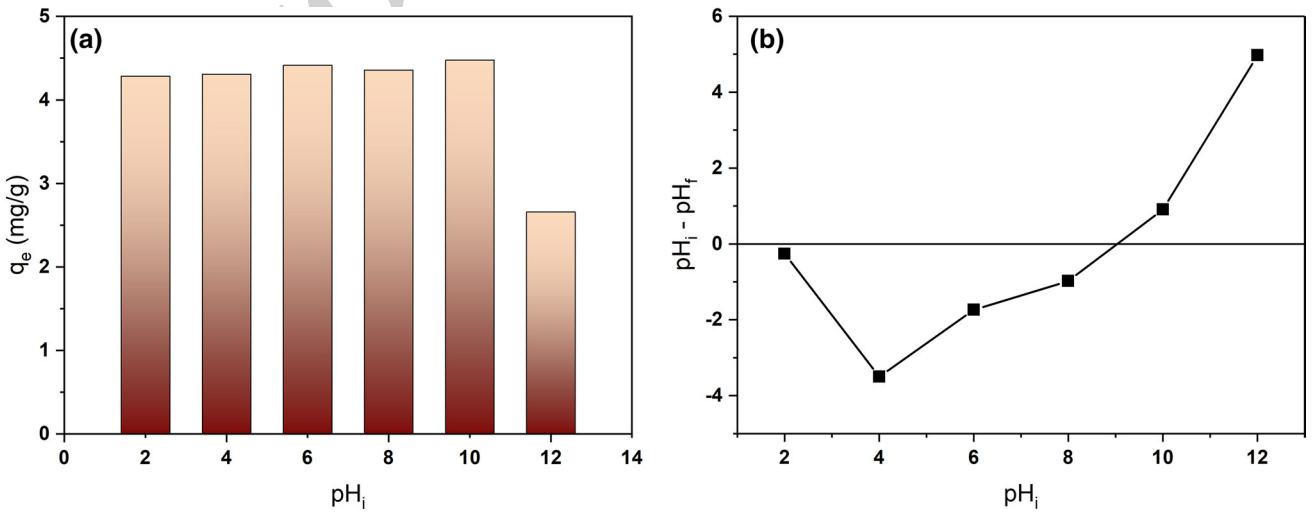

Fig. 1 **a** Effect of pHi on adsorption capacity; and **b** Experimental solid-addition technique curve for Fe-BTC used to determine pH_{PZC}

These results are in line with experimental investigations previously reported in the literature for the adsorption of MO and other dyes on different MOFs (Haque et al. 2010, 2011; Huo and Yan 2012; Chen et al. 2012). Also, it can be noticed in Figure S6 that the removal efficiency (*RE*) decreases with increasing initial concentration. This can be attributed to the fact that at the same amount of adsorbent, increasing C_o leads to a higher equilibrium concentration of MO due to the higher amount of the dye molecules in the liquid phase. Consequently, the difference between C_o and C_e will decrease, leading to a decrease in the removal efficiency.

The effect of changing adsorbent dosage at constant MO concentration was also investigated. It is anticipated that increasing Fe-BTC dosage decreases the MO uptake per gram of adsorbent due to the change in Fe-BTC to MO concentrations ratios. At an initial MO concentration of 15 mg/L, increasing Fe-BTC dosage from 50 to 200 mg decreased MO uptake from 10.3 to 3.43 mg/g, as shown in Figure S7. On the other hand, the opposite trend is noticed for the removal efficiency of MO; as the adsorbent dosage increases, the dye removal efficiency increases as well. At high Fe-BTC to MO ratio (i.e., higher adsorbent dosage), there is a very fast superficial adsorption onto the surface of the adsorbent leading to lower MO concentration compared to the lower Fe-BTC to MO concentration ratio (i.e., lower adsorbent dosage) (Senthil Kumar et al. 2010; Yao et al. 2011; Abdi et al. 2017). In other words, increasing adsorbent dosage leads to decreasing the concentration gradient between MO concentration in the solution and MO concentration on the adsorbent surface. This also explains the higher removal efficiency for the higher Fe-BTC dosage, as removal efficiency is calculated from the difference between the initial and final MO concentrations in the solution.

Adsorption kinetics

The rate of the adsorption process of MO on Fe-BTC was studied over a contact time of 180 min. The obtained kinetic data were fitted to three models, Elovich, PSO, and PFO, and the calculated kinetic models' parameters, along with their corresponding R^2, RMSE, and SSE, are summarized in Table S1. The results in Fig. 2 indicate that the Elovich model provides a better fit for the data than PSO, while the PFO model had the lowest fitting accuracy among the three models. The $q_{e,calc}$ values from the PSO model (Table S1) show good agreement with $q_{e,exp}$, while the rate constant of PSO decreases with increasing initial MO concentration. Similar trends have been reported in the literature for the adsorption of MO and other dyes on various MOFs (Chen et al. 2012; Tong et al. 2013; Wu et al. 2017). On the other hand, the high R^2 values and the low RMSE *and* SSE values obtained for the Elovich model suggest that MO adsorption

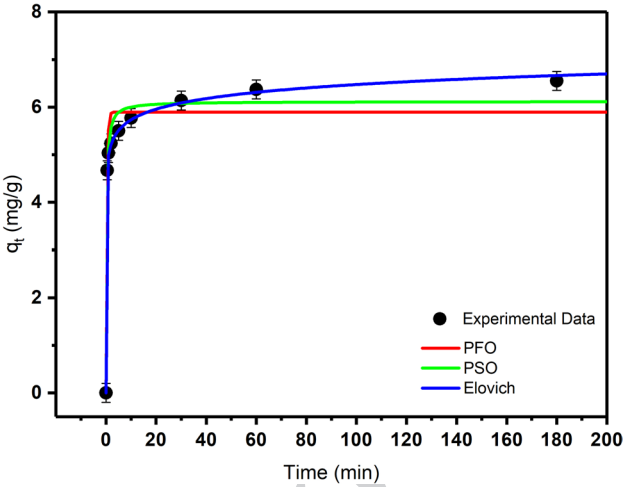

Fig. 2 Kinetic models fitted to the experimental data ($m = 100$, $C_o = 15$ mg/L)

on Fe-BTC is heterogeneous (Teng and Hsieh 1999; Piasecki and Rudziński 2007).

In order to analyze the effect of intraparticle diffusion on the rate of the adsorption process, the kinetic data at three different initial MO concentrations were fitted to the IPD model. The fitted experimental data (Figure S8), reveals that q_t at different initial concentrations exhibits a trilinear adsorption behavior, implying the existence of three successive adsorption stages (Wu et al. 2009; Machado et al. 2012). Each straight line represents a single stage in a three-step adsorption mechanism, which are: (1) MO molecules diffusion through the liquid/solid boundary to adsorb on the MOF's surface; (2) intraparticle diffusion of MO molecules; and (3) an equilibrium stage is reached as the MOF approaches saturation (Wu et al. 2009).

Adsorption isotherms

The thermodynamics of the adsorption process was also investigated, and the obtained adsorption isotherms were fitted to four models at three temperatures, as summarized in Table S2. It is evident by observing the trend of the nonlinear plots in Fig. 3 that among the four isotherm models fitted to the experimental data of q_e versus C_e at 298 K, Langmuir model is the best fitting model with highest R^2 and lowest RMSE and SSE (Table S2). This indicates that the adsorption process is through the formation of a monolayer of the adsorbate on a homogenous surface of the adsorbent. On the other hand, the Langmuir separation factor (R_L) as a function of C_o at 298, 303, and 313 K (Figure S9) shows that $0 < R_L < 1$, signaling a favorable adsorption process (Baccar et al. 2010). The values of R_L decreased as the temperature increased, demonstrating an increased adsorption efficacy at higher temperatures (Baccar et al. 2010). These results

Journal : Large 13762 | Article No : 3103 | Pages : 16 | MS Code : 3103 | Dispatch : 28-12-2020

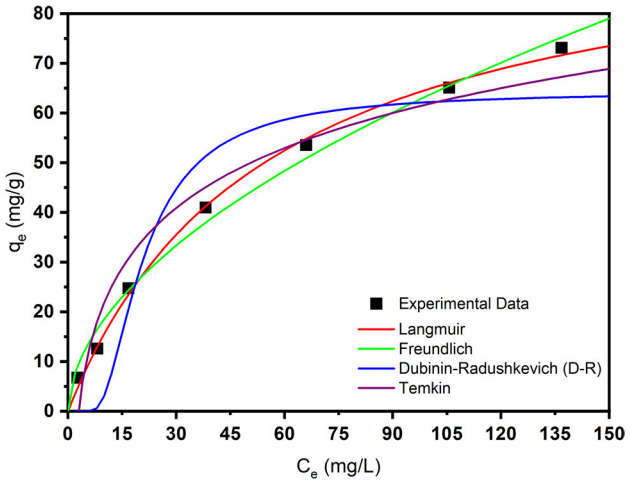

Fig. 3 Equilibrium adsorption isotherms of MO adsorption on Fe-BTC at 298 K

are per the findings that the calculated q_m from Langmuir isotherm (Table S2) increases as temperature increases.

Further analysis into the other models' parameters shows that all of the n values in Freundlich isotherm were greater than unity, which means $(1/n) < 1$; hence, MO adsorption on Fe-BTC is favorable (Baccar et al. 2010). At higher temperatures (303 and 313 K), all employed isotherm models had a good agreement between the experimental and predicted data ($R^2 > 0.96$). Finally, the values of the mean adsorption energy (E) calculated from the D–R isotherm (Table S2) suggest that MO adsorption proceeds through physical route (Vijayaraghavan et al. 2006).

Adsorption thermodynamics

To further analyze the thermodynamic data for MO adsorption on Fe-BTC, the Van't Hoff plot (Figure S10) was constructed and the changes in free energy ($\Delta G°$), enthalpy ($\Delta H°$) and entropy ($\Delta S°$) (Table S3) were determined. The results show that the adsorption is spontaneous with a negative $\Delta G°$ but endothermic since $\Delta H°$ (16.86 kJ mol^{-1}) is positive (Liu and Liu 2008). The endothermic behavior suggests that increasing temperature could improve the mobility of MO molecules from the solution toward Fe-BTC surface, and at the same time, increases the desorption of water molecules and anions to free the active sites of the MOF for binding of MO (Mahmoodi and Najafi 2012). This desorption also explains the positive value of $\Delta S°$ (162.4 J mol^{-1} K^{-1}), which reflects that the system experiences an increased disorder at the solution/MOF boundary (Baccar et al. 2010); hence, MO adsorption on Fe-BTC is an entropy-driven process (Haque et al. 2010). Furthermore, the endothermic adsorption of MO (Haque et al. 2010, 2011, 2014; Shen et al. 2015; Wu et al. 2017; Abdi et al. 2017) with a value of $\Delta H°$ less than 40 kJ mol^{-1} is an indication of a physical adsorption mechanism (Kara et al. 2003; Angin 2014).

Fixed-bed column adsorption

The removal efficiency and adsorption capacity of MO using Fe-BTC obtained from the batch experiments are useful to determine the MOF's effectiveness under the considered experimental conditions. The batch experiments also provide a fundamental understanding of the MO adsorption mechanism, kinetic parameters, and the optimum process conditions. However, the data may not be applied to the continuous column operation because they are often difficult to use directly in the design and scale-up of fixed-bed columns since a continuous flow column is not at equilibrium (Agrawal and Bajpai 2011; Sadaf and Bhatti 2014). Therefore, fixed-bed experiments are more useful for the scale-up of the adsorption process. The essential criterion in the design of the adsorption system is the service time, known as column breakthrough. The breakthrough time and the shape of the concentration–time profile are essential for the design of an adsorption column.

In this section, the performance of MO adsorption in a Fe-BTC fixed-bed column is reported at two bed depths (0.75 and 1.5 cm). Based on the results of the batch experiments, the pH of the MO solution was maintained at 6, and the experiments were carried out at room temperature. Also, the influent MO concentration was selected as 15 mg/L at 4.5 mL/h constant flow rate.

Fixed-bed column performance

Figure 4 presents both types of breakthrough curves (BTCs) obtained from MO adsorption on Fe-BTC for different bed depths. The calculated fixed-bed parameters are presented in Table 1. The results revealed that increasing the bed depth leads to an increase in the breakthrough and exhaustion times, as evidenced by the right shift of the BTCs. By expanding the bed depth, the total amount of adsorbed MO in the fixed-bed (m_{ad}), the removal efficiency (RE_{bed}), and the maximum bed adsorption capacity (q_{max}) also increased. An increase in the empty bed contact time (EBCT), mass transfer zone (MTZ), and $t_{50\%}$ (time required for 50% breakthrough) was also observed.

Furthermore, the measured volume of the treated effluent at breakthrough ($V_{treated}$) increased as the bed depth increased. These results are expected; as bed depth is increased, the available surface area of Fe-BTC in the column (i.e., adsorption sites) is also increased, which means larger q_{max} and higher RE_{bed} (Du et al. 2018). Moreover, with longer bed depth, the contact time in the bed is increased, and in turn, EBCT increased, which means more volume of effluent can be treated (Du et al. 2018). Similar observations

Journal : Large 13762 | Article No : 3103 | Pages : 16 | MS Code : 3103 | Dispatch : 28-12-2020

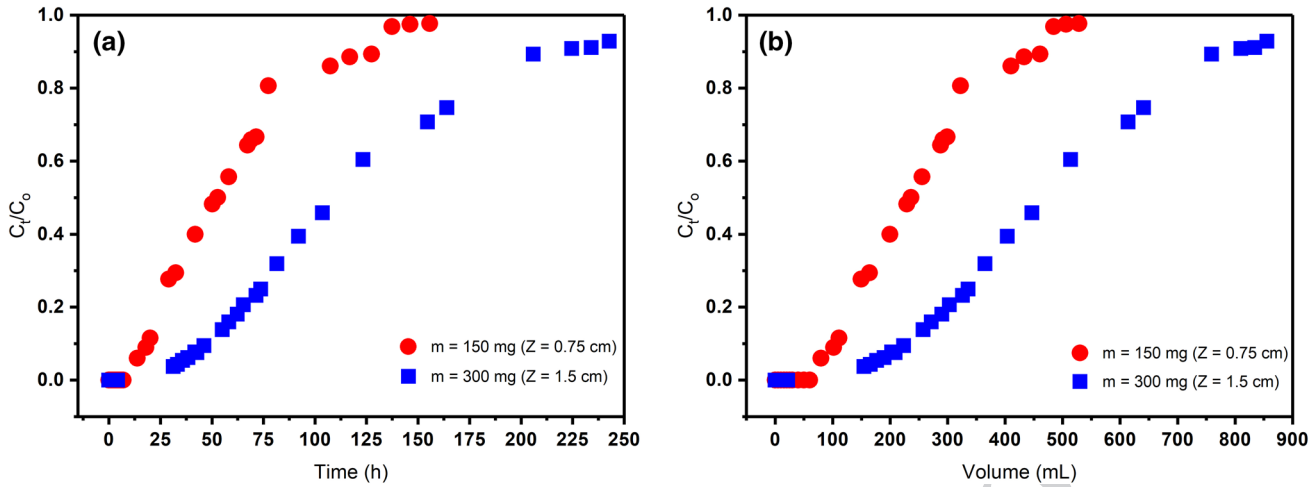

Fig. 4 BTCs of MO adsorption on Fe-BTC fixed-bed column as function of **a** time and **b** treated volume (C_o = 15 mg/L, Q = 4.5 mL/h)

Table 1 Fixed-bed column parameters obtained at different bed depths (C_o = 15 mg/L, Q = 4.5 mL/h)

Bed Depth (cm)	t_b (h)	t_e (h)	m_{ad} (mg)	m_{tot} (mg)	RE_{bed} (%)	q_{max} (mg/g)	EBCT (min)	MTZ (cm)	$V_{treated}$ (mL)	$t_{50\%}$ (h)
0.75	20.0	127.5	3.03	8.61	35.2	20.2	7.85	0.63	106	52.8
1.50	46.2	205.9	6.49	13.9	46.7	21.6	15.7	1.16	228	109.2

were reported in the literature (Tan et al. 2008; Han et al. 2009).

Adsorption performance in batch vs. fixed-bed column

In practical water/wastewater treatment applications, a fixed-bed column configuration is usually preferred over the batch configuration. To illustrate this point; the performance of MO adsorption on Fe-BTC in batch and fixed-bed column configurations is compared at the following conditions: (1) MO initial concentration is 15 mg/L, (2) Fe-BTC dosage is 150 mg, (3) pH is 6 (normal pH without adjustment), and (4) the temperature is 25 °C.

The results from the batch adsorption experiments at the aforementioned conditions showed that the final removal efficiency was around 97% (see Figure S7), which corresponds to normalized concentration (C/C_o) of 0.03, while the total volume of the treated MO solution was 50 mL. Interestingly, when the fixed-bed column configuration was utilized, the value of C/C_o for the same volume of treated MO solution was zero (see Fig. 4b). Furthermore, to reuse the treated water in the batch mode, an additional separation step had to be implemented to separate the liquid from the solid, contrary to the column mode where the adsorbent packing was fixed in the column, while the liquid passed through the bed. These findings demonstrate the advantage of the fixed-bed configuration over the batch configuration.

Kinetic modeling of fixed-bed column breakthrough

Empirical breakthrough models The relative change in the concentration of MO to the original concentration over time (C_t/C_o) was fitted to four models whose calculated parameters are summarized in Table 2. It was found that Thomas and Y-N models had the same fitting coefficients (R^2, RMSE, and SSE), but the Clark model was marginally better while the MDR model had the best fitting coefficients (highest R^2 and lowest RMSE, and SSE). The experimental and the MDR-predicted BTCs at different bed depths are shown in Fig. 5.

The results of the Thomas model showed that q_{TH} increased as the bed depth increased, while K_{TH} decreased, which can be explained by the additional available adsorption sites when bed depth is increased, consequently resulting in longer breakthrough time (Chu 2010; Cruz-Olivares et al. 2013). Similarly, K_{YN} decreased with an increase in bed depth, whereas the value of τ increased. The increase in τ is expected since larger bed depth will increase contact time in the bed as manifested by the rise in EBCT, leading to a longer breakthrough time and subsequently longer time to reach a 50% breakthrough (Xu et al. 2013; Podder and Majumder 2016). In addition, it can be noticed that the values of τ in Table 2 were satisfactorily close to the experimentally determined $t_{50\%}$ presented in Table 1. Finally, the results of the Clark model showed that the value of A

Journal : Large 13762 | Article No : 3103 | Pages : 16 | MS Code : 3103 | Dispatch : 28-12-2020

Table 2 Summary of the calculated parameters of the kinetic models at different bed depths

BTC Model	Parameters	Z (cm)	
		0.75	1.50
Thomas	q_{TH} (mg g^{-1})	24.58	25.97
	K_{TH} (mL mg^{-1} h^{-1})	3.732	1.972
	R^2	0.980	0.986
	RMSE	0.054	0.039
	SSE	0.080	0.049
Yoon–Nelson (Y–N)	K_{YN} (h^{-1})	0.056	0.030
	τ (h)	54.6	115.4
	R^2	0.980	0.986
	RMSE	0.054	0.039
	SSE	0.080	0.049
Clark	A	14.38	20.25
	r (h^{-1})	0.053	0.028
	R^2	0.982	0.988
	RMSE	0.052	0.036
	SSE	0.072	0.042
Modified Dose Response (MDR)	q_{MDR} (mg g^{-1})	22.39	24.14
	a_{MDR}	2.344	2.801
	R^2	0.995	0.999
	RMSE	0.028	0.012
	SSE	0.021	0.004

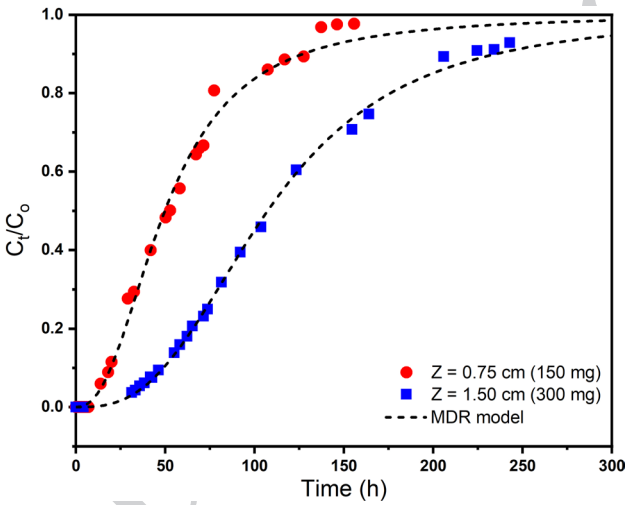

Fig. 5 Comparison between the experimental and the predicted BTCs

increased with increasing bed depth while the value of r decreased.

On the other hand, the calculated maximum adsorption capacity from the MDR model (q_{MDR}) increased with the increase in the bed depth, similar to the Thomas model, and the value of a_{MDR} increased as well. The calculated q_{MDR} values were well close to the experimentally determined maximum bed adsorption capacity (q_{max}). Finally, it was noticed that at the initial operating time, the predicted C_t/C_o values from the Thomas, Y–N, and Clark models were all greater than zero, which is not in agreement with the experimental data. The MDR model was the only one to fit the experimental data at the initial operating time when the values of C_t/C_o were zero or very close to zero. This finding is significant since overestimating C_t/C_o leads to predicting that the breakthrough time is reached prematurely, which is undesirable in the operation of a fixed-bed column because the actual column capacity will not be fully utilized (Yan et al. 2001).

Analytical solution of the dynamic advection–dispersion–adsorption model In order to confirm the validity of the linear adsorption isotherm assumption, the equilibrium isotherm data at 298 K from the batch experiments at low MO concentration range were fitted to Eq. (29). The results in Figure S12 reveal that the adsorption can be expressed by the linear isotherm model in the low concentration range (R^2 is 0.950), while the Langmuir model fits the complete range of MO concentrations (as shown in the batch adsorption isotherms section). Also, the initial MO concentration used in the fixed-bed experiments was 15 mg/L, which is in the low concentration range; thus, the assumption of linear adsorption isotherm is reasonable to be used in the solution of the breakthrough model. In addition, the value of K_p calculated from the linear isotherm was found to be 1.513 L/g.

It is evident that the experimental breakthrough data fitted well the analytical model at both bed depths (as shown in Fig. 6) with $R^2 > 0.99$ and low RMSE and *SSE* values, which are presented in Table 3. The results show that D_{eff} increased as the bed depth increased, which suggests that the axial dispersion of the fluid in the column is significantly

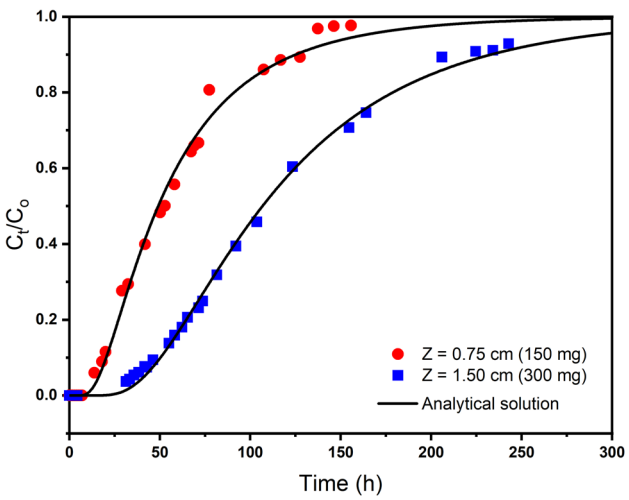

Fig. 6 The analytical solution model fitted to the experimental breakthrough data

Journal : Large 13762 | Article No : 3103 | Pages : 16 | MS Code : 3103 | Dispatch : 28-12-2020

Table 3 Summary of the calculated model parameters at different bed depths

Z (cm)	Parameters			R^2	RMSE	SSE
	K_P (L/g)	D_{eff} (cm^2/s)	D_L (cm^2/s)			
0.75	1.069	7.56×10^{-7}	1.04×10^{-3}	0.9949	0.0274	0.0203
1.50	1.076	1.01×10^{-6}	1.39×10^{-3}	0.9977	0.0155	0.0079

impacted by the change in bed depth, which influences the adsorption performance of the column. Also, the values of D_{eff} were converted to the longitudinal dispersion coefficient (D_L) by multiplying with R_f (Table 3), which are useful in the scale-up and design of the fixed-bed adsorption column for MO removal from water. Furthermore, the values of K_P calculated at both bed depths are of the same order of magnitude as the one calculated from the batch-scale experiments (Figure S12), which indicate that the linear isotherm assumption is valid at the lower MO concentration range, and that the performance of MO adsorption is similar in both systems. The slightly higher values of K_P in the batch experiments compared to the column experiments suggest that Fe-BTC/MO equilibrium is better achieved in the batch system.

The analytical model was utilized to predict the influence of bed depth (Z) on the breakthrough curve. For this purpose, a 3D surface plot representing the breakthrough curves (BTCs) for bed depth between 0 and 5 cm and operating time from 0 to 300 h was generated from the model based on the calculated parameters using OriginPro (2020, version 9.7). Also, the experimental BTCs were superimposed on the 3D surface to illustrate the matching between the predicted and measured BTCs. The 3D surface plot in Fig. 7a represents the BTC of MO adsorption on Fe-BTC in the fixed-bed column, which can be useful for the prediction of adsorption BTCs at different bed depths. Besides, Fig. 7b represents the contour plot generated from the 3D surface plot in which each line is equivalent to the corresponding C/C_o on each BTC on the surface (0.1 is for t_b, and 0.9 is for t_e). It can be noticed that as bed depth increases, the gap between the lines representing breakthrough and exhaustion times increases as well, signaling the broadening of the BTC and increase in breakthrough and exhaustion times. This can be attributed to the expansion of the MTZ resulting from the increase in the available surface area of Fe-BTC in the column.

In addition, the analytical model was used to analyze the mass transfer zone (MTZ) along the length of the column. This was done by setting C/C_o at 0.1 and 0.9, and then solving for t_b and t_e, respectively. The model was solved at bed depths from 0 to 500 cm and the determined t_b and t_e values were used to calculate the length of the MTZ corresponding to each bed depth using Eq. (6). Then, the calculated lengths of MTZ were plotted against the corresponding bed depths. Figure S13 illustrates that as the bed depth increases, the length of the mass transfer zone increases, which is consistent with the findings from the experimental results. Also, it can be seen that the relation between the length of MTZ and bed depth is not linear, which is also in agreement with previously reported studies (Naja and Volesky 2006; Apiratikul 2020).

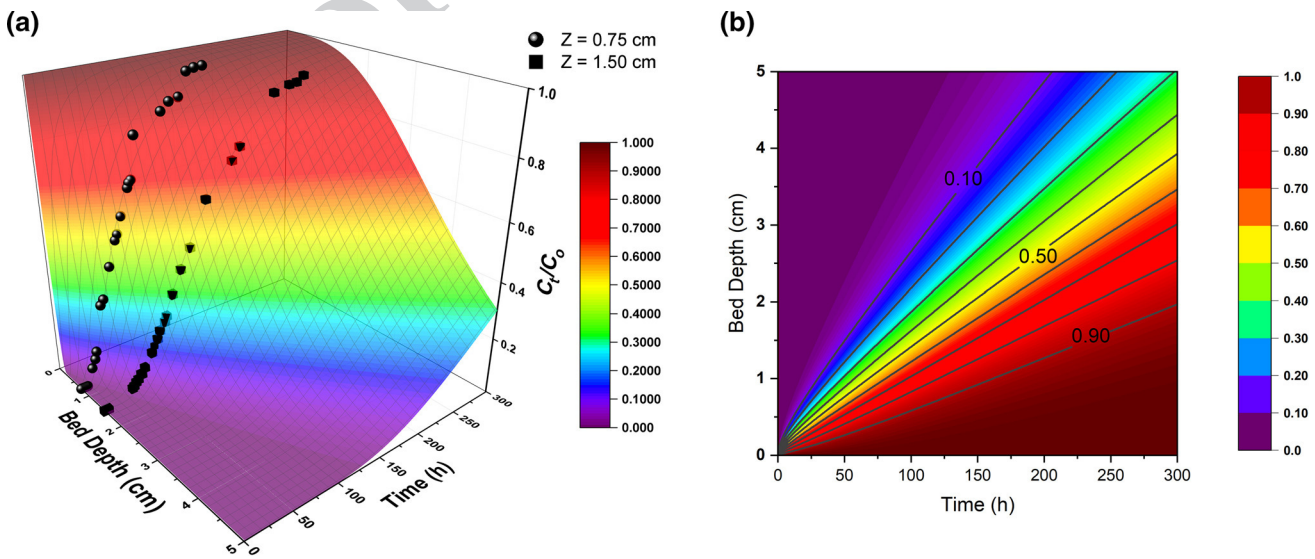

Fig. 7 **a** 3D surface plot of MO adsorption on Fe-BTC. **b** Contour plot for MO adsorption on Fe-BTC

Journal : Large 13762 | Article No : 3103 | Pages : 16 | MS Code : 3103 | Dispatch : 28-12-2020

Conclusion

In conclusion, Fe-BTC was proven to be an efficient adsorbent to be utilized for the removal of methyl orange from aqueous solution in both batch and continuous setups under several experimental conditions. The kinetic analysis showed that the adsorption of MO onto Fe-BTC was rapid, and the equilibrium was reached in 60 min. The pH experiments revealed that Fe-BTC could be used over a wide range of pH and maintain high removal efficiency and adsorption capacity. Also, the maximum adsorption capacity reached 114 mg/g at 313 K. In addition, it was found that the adsorption process follows the Elovich model ($R^2 > 0.99$), while, according to the isotherm analysis, the Langmuir isotherm was the best to describe the equilibrium data ($R^2 > 0.99$). Moreover, thermodynamic parameters indicated that the adsorption process was spontaneous (ΔG° was consistently negative), endothermic (ΔH° was 16.86 kJ mol^{-1}), and entropically favored with ΔS° of 162.4 J mol^{-1} K^{-1}. Furthermore, electrostatic interactions and π–π stacking/interaction were concluded to be the primary mechanisms in MO adsorption on Fe-BTC. The fixed-bed column results showed the breakthrough time at 0.75 cm bed depth was 20.0 h while at 1.5 cm, it was 46.2 h. Also, increasing the bed depth increased bed removal efficiency and the column's maximum adsorption capacity. The analysis of the breakthrough experimental data showed that MDR is the best model to predict the breakthrough curve. In addition, the analytical model obtained from the solution of the advection–dispersion–adsorption mass transfer partial differential equation illustrated excellent fitting to the experimental BTC data. The model was also utilized to construct a 3D surface plot that can be used to predict the BTC at different bed depths. Moreover, the desorption experiments revealed that Fe-BTC was easily regenerated by a simple washing using ethanol at room temperature. Finally, it has been demonstrated that the iron-based metal–organic framework has excellent potential for industrial-scale adsorption applications.

Acknowledgements The authors gratefully acknowledge the financial support by the American University of Sharjah Enhanced Faculty Research Grant EFRG18-BBR-CEN-03.

Compliance with ethical standards

conflict of interest The authors declare that they have no conflict of interest.

References

Abdi J, Vossoughi M, Mahmoodi NM, Alemzadeh I (2017) Synthesis of metal–organic framework hybrid nanocomposites based on GO and CNT with high adsorption capacity for dye removal. Chem Eng J 326:1145–1158. https://doi.org/10.1016/j.cej.2017.06.054

Adeyemo AA, Adeoye IO, Bello OS (2012) Metal organic frameworks as adsorbents for dye adsorption: overview, prospects and future challenges. Toxicol Environ Chem 94:1846–1863. https://doi.org/10.1080/02772248.2012.744023

Agrawal P, Bajpai AK (2011) Dynamic column adsorption studies of toxic Cr(VI) ions onto iron oxide loaded gelatin nanoparticles. J Dispers Sci Technol 32:1353–1362. https://doi.org/10.1080/01932691.2010.505871

Aguilera-Sigalat J, Bradshaw D (2016) Synthesis and applications of metal–organic framework–quantum dot (QD@MOF) composites. Coord Chem Rev 307:267–291. https://doi.org/10.1016/j.ccr.2015.08.004

Angin D (2014) Utilization of activated carbon produced from fruit juice industry solid waste for the adsorption of Yellow 18 from aqueous solutions. Bioresour Technol 168:259–266. https://doi.org/10.1016/j.biortech.2014.02.100

Apiratikul R (2020) Application of analytical solution of advection–dispersion–reaction model to predict the breakthrough curve and mass transfer zone for the biosorption of heavy metal ion in a fixed bed column. Process Saf Environ Prot 137:58–65. https://doi.org/10.1016/j.psep.2020.02.018

Arora C, Soni S, Sahu S et al (2019) Iron based metal organic framework for efficient removal of methylene blue dye from industrial waste. J Mol Liq 284:343–352. https://doi.org/10.1016/j.molliq.2019.04.012

Arslan M, Ullah I, Müller JA, et al (2017) Organic micropollutants in the environment: ecotoxicity potential and methods for remediation. In: Enhancing cleanup of environmental pollutants. Volume 1: biological approaches. Springer International Publishing, Cham, Switzerland, pp 65–99

Ayati A, Shahrak MN, Tanhaei B, Sillanpää M (2016) Emerging adsorptive removal of azo dye by metal–organic frameworks. Chemosphere 160:30–44. https://doi.org/10.1016/j.chemosphere.2016.06.065

Baccar R, Blánquez P, Bouzid J et al (2010) Equilibrium, thermodynamic and kinetic studies on adsorption of commercial dye by activated carbon derived from olive-waste cakes. Chem Eng J 165:457–464. https://doi.org/10.1016/j.cej.2010.09.033

Basar C (2006) Applicability of the various adsorption models of three dyes adsorption onto activated carbon prepared waste apricot. J Hazard Mater 135:232–241. https://doi.org/10.1016/j.jhazmat.2005.11.055

Centrone A, Santiso EE, Hatton TA (2011) Separation of chemical reaction intermediates by metal–organic frameworks. Small 7:2356–2364. https://doi.org/10.1002/smll.201100098

Chen C, Zhang M, Guan Q, Li W (2012) Kinetic and thermodynamic studies on the adsorption of xylenol orange onto MIL-101(Cr). Chem Eng J 183:60–67. https://doi.org/10.1016/j.cej.2011.12.021

Chu KH (2010) Fixed bed sorption: setting the record straight on the Bohart–Adams and Thomas models. J Hazard Mater 177:1006–1012. https://doi.org/10.1016/j.jhazmat.2010.01.019

Clark RM (1987) Evaluating the cost and performance of field-scale granular activated carbon systems. Environ Sci Technol 21:573–580. https://doi.org/10.1021/es00160a008

Cruz-Olivares J, Pérez-Alonso C, Barrera-Díaz C et al (2013) Modeling of lead (II) biosorption by residue of allspice in a fixed-bed column. Chem Eng J 228:21–27. https://doi.org/10.1016/j.cej.2013.04.101

Dhaka S, Kumar R, Deep A et al (2019) Metal–organic frameworks (MOFs) for the removal of emerging contaminants from aquatic environments. Coord Chem Rev 380:330–352. https://doi.org/10.1016/j.ccr.2018.10.003

Dhakshinamoorthy A, Alvaro M, Horcajada P et al (2012) Comparison of porous iron trimesates basolite F300 and MIL-100(Fe) as heterogeneous catalysts for lewis acid and oxidation reactions: roles of structural defects and stability. ACS Catal 2:2060–2065. https://doi.org/10.1021/cs300345b

Dias EM, Petit C (2015) Towards the use of metal–organic frameworks for water reuse: a review of the recent advances in the field of organic pollutants removal and degradation and the next steps in the field. J Mater Chem A 3:22484–22506. https://doi.org/10.1039/C5TA05440K

Dichiara AB, Harlander SF, Rogers RE (2015) Fixed bed adsorption of diquat dibromide from aqueous solution using carbon nanotubes. RSC Adv 5:61508–61512. https://doi.org/10.1039/C5RA11167F

Du Z, Zheng T, Wang P (2018) Experimental and modelling studies on fixed bed adsorption for Cu(II) removal from aqueous solution by carboxyl modified jute fiber. Powder Technol 338:952–959. https://doi.org/10.1016/j.powtec.2018.06.015

Farha OK, Eryazici I, Jeong NC et al (2012) Metal–organic framework materials with ultrahigh surface areas: is the sky the limit? J Am Chem Soc 134:15016–15021. https://doi.org/10.1021/ja3055639

Fiol N, Villaescusa I (2009) Determination of sorbent point zero charge: usefulness in sorption studies. Environ Chem Lett 7:79–84. https://doi.org/10.1007/s10311-008-0139-0

Furukawa H, Go YB, Ko N et al (2011) Isoreticular expansion of metal–organic frameworks with triangular and square building units and the lowest calculated density for porous crystals. Inorg Chem 50:9147–9152. https://doi.org/10.1021/ic201376t

Furukawa H, Cordova KE, O'Keeffe M, Yaghi OM (2013) The chemistry and applications of metal–organic frameworks. Science 80(341):1230444

Ghaedi M, Ghaedi AM, Negintaji E et al (2014) Random forest model for removal of bromophenol blue using activated carbon obtained from *Astragalus bisulcatus* tree. J Ind Eng Chem 20:1793–1803. https://doi.org/10.1016/j.jiec.2013.08.033

Han R, Wang Y, Zhao X et al (2009) Adsorption of methylene blue by phoenix tree leaf powder in a fixed-bed column: experiments and prediction of breakthrough curves. Desalination 245:284–297. https://doi.org/10.1016/j.desal.2008.07.013

Haque E, Lee JE, Jang IT et al (2010) Adsorptive removal of methyl orange from aqueous solution with metal–organic frameworks, porous chromium-benzenedicarboxylates. J Hazard Mater 181:535–542. https://doi.org/10.1016/j.jhazmat.2010.05.047

Haque E, Jun JW, Jhung SH (2011) Adsorptive removal of methyl orange and methylene blue from aqueous solution with a metal–organic framework material, iron terephthalate (MOF-235). J Hazard Mater 185:507–511. https://doi.org/10.1016/j.jhazmat.2010.09.035

Haque E, Lo V, Minett AI et al (2014) Dichotomous adsorption behaviour of dyes on an amino-functionalised metal–organic framework, amino-MIL-101(Al). J Mater Chem A 2:193–203. https://doi.org/10.1039/C3TA13589F

Hasan Z, Jhung SH (2015) Removal of hazardous organics from water using metal–organic frameworks (MOFs): plausible mechanisms for selective adsorptions. J Hazard Mater 283:329–339. https://doi.org/10.1016/j.jhazmat.2014.09.046

He X, Deng F, Shen T et al (2019) Exceptional adsorption of arsenic by zirconium metal–organic frameworks: engineering exploration and mechanism insight. J Colloid Interface Sci 539:223–234. https://doi.org/10.1016/j.jcis.2018.12.065

Hosseini S, Khan MA, Malekbala MR et al (2011) Carbon coated monolith, a mesoporous material for the removal of methyl orange from aqueous phase: adsorption and desorption studies. Chem Eng J 171:1124–1131. https://doi.org/10.1016/j.cej.2011.05.010

Huo S-H, Yan X-P (2012) Metal–organic framework MIL-100(Fe) for the adsorption of malachite green from aqueous solution. J Mater Chem 22:7449. https://doi.org/10.1039/c2jm16513a

Jia Y, Jin Q, Li Y et al (2015) Investigation of the adsorption behaviour of different types of dyes on MIL-100(Fe) and their removal from natural water. Anal Methods 7:1463–1470. https://doi.org/10.1039/C4AY02726D

Joseph L, Jun B-M, Jang M et al (2019) Removal of contaminants of emerging concern by metal–organic framework nanoadsorbents: a review. Chem Eng J 369:928–946. https://doi.org/10.1016/j.cej.2019.03.173

Kara M, Yuzer H, Sabah E, Celik M (2003) Adsorption of cobalt from aqueous solutions onto sepiolite. Water Res 37:224–232. https://doi.org/10.1016/S0043-1354(02)00265-8

Karami A, Sabouni R, Ghommem M (2020) Experimental investigation of competitive co-adsorption of naproxen and diclofenac from water by an aluminum-based metal–organic framework. J Mol Liq 305:112808. https://doi.org/10.1016/j.molliq.2020.112808

Khan NA, Hasan Z, Jhung SH (2013) Adsorptive removal of hazardous materials using metal–organic frameworks (MOFs): a review. J Hazard Mater 244–245:444–456. https://doi.org/10.1016/j.jhazmat.2012.11.011

Kousha M, Daneshvar E, Sohrabi MS et al (2012) Adsorption of acid orange II dye by raw and chemically modified brown macroalga *Stoechospermum marginatum*. Chem Eng J 192:67–76. https://doi.org/10.1016/j.cej.2012.03.057

Langmuir I (1918) The adsorption of gases on plane surfaces of glass, mica and platinum. J Am Chem Soc 40:1361–1403. https://doi.org/10.1021/ja02242a004

Liu Y, Liu Y-J (2008) Biosorption isotherms, kinetics and thermodynamics. Sep Purif Technol 61:229–242. https://doi.org/10.1016/j.seppur.2007.10.002

Liu X, Zhou Y, Zhang J et al (2017) Iron containing metal–organic frameworks: structure, synthesis, and applications in environmental remediation. ACS Appl Mater Interfaces 9:20255–20275. https://doi.org/10.1021/acsami.7b02563

Liu W, Shen X, Han Y et al (2019) Selective adsorption and removal of drug contaminants by using an extremely stable Cu(II)-based 3D metal–organic framework. Chemosphere 215:524–531. https://doi.org/10.1016/j.chemosphere.2018.10.075

Luo Y, Guo W, Ngo HH et al (2014) A review on the occurrence of micropollutants in the aquatic environment and their fate and removal during wastewater treatment. Sci Total Environ 473–474:619–641. https://doi.org/10.1016/j.scitotenv.2013.12.065

Machado FM, Bergmann CP, Lima EC et al (2012) Adsorption of Reactive Blue 4 dye from water solutions by carbon nanotubes:

experiment and theory. Phys Chem Chem Phys 14:11139. https://doi.org/10.1039/c2cp41475a

Mahmoodi NM, Najafi F (2012) Synthesis, amine functionalization and dye removal ability of titania/silica nano-hybrid. Microporous Mesoporous Mater 156:153–160. https://doi.org/10.1016/j.micromeso.2012.02.026

Mittal A, Malviya A, Kaur D et al (2007) Studies on the adsorption kinetics and isotherms for the removal and recovery of Methyl Orange from wastewaters using waste materials. J Hazard Mater 148:229–240. https://doi.org/10.1016/j.jhazmat.2007.02.028

Naja G, Volesky B (2006) Behavior of the mass transfer zone in a biosorption column. Environ Sci Technol 40:3996–4003. https://doi.org/10.1021/es051542p

Ogata A, Banks RB (1961) A solution of the differential equation of longitudinal dispersion in porous media (U.S. Geological Survey Professional Paper 411-A). Fluid movement in earth materials. Washington, D.C

Park EY, Hasan Z, Khan NA, Jhung SH (2013) Adsorptive removal of bisphenol-A from water with a metal–organic framework, a porous chromium-benzenedicarboxylate. J Nanosci Nanotechnol 13:2789–2794. https://doi.org/10.1166/jnn.2013.7411

Piasecki W, Rudziński W (2007) Application of the statistical rate theory of interfacial transport to investigate the kinetics of divalent metal ion adsorption onto the energetically heterogeneous surfaces of oxides and activated carbons. Appl Surf Sci 253:5814–5817. https://doi.org/10.1016/j.apsusc.2006.12.066

Podder MS, Majumder C (2016) Fixed-bed column study for As(III) and As(V) removal and recovery by bacterial cells immobilized on Sawdust/$MnFe_2O_4$ composite. Biochem Eng J 105:114–135. https://doi.org/10.1016/j.bej.2015.09.008

Qin F-X, Jia S-Y, Liu Y et al (2015) Adsorptive removal of bisphenol A from aqueous solution using metal–organic frameworks. Desalin Water Treat 54:93–102. https://doi.org/10.1080/19443994.2014.883331

Sadaf S, Bhatti HN (2014) Evaluation of peanut husk as a novel, low cost biosorbent for the removal of Indosol Orange RSN dye from aqueous solutions: batch and fixed bed studies. Clean Technol Environ Policy 16:527–544. https://doi.org/10.1007/s10098-013-0653-z

Samokhvalov A (2018) Aluminum metal–organic frameworks for sorption in solution: a review. Coord Chem Rev 374:236–253. https://doi.org/10.1016/j.ccr.2018.06.011

Senthil Kumar P, Ramalingam S, Senthamarai C et al (2010) Adsorption of dye from aqueous solution by cashew nut shell: studies on equilibrium isotherm, kinetics and thermodynamics of interactions. Desalination 261:52–60. https://doi.org/10.1016/j.desal.2010.05.032

Shen T, Luo J, Zhang S, Luo X (2015) Hierarchically mesostructured MIL-101 metal–organic frameworks with different mineralizing agents for adsorptive removal of methyl orange and methylene blue from aqueous solution. J Environ Chem Eng 3:1372–1383. https://doi.org/10.1016/j.jece.2014.12.006

Tan KL, Hameed BH (2017) Insight into the adsorption kinetics models for the removal of contaminants from aqueous solutions. J Taiwan Inst Chem Eng 74:25–48. https://doi.org/10.1016/j.jtice.2017.01.024

Tan IAW, Ahmad AL, Hameed BH (2008) Adsorption of basic dye using activated carbon prepared from oil palm shell: batch and fixed bed studies. Desalination 225:13–28. https://doi.org/10.1016/j.desal.2007.07.005

Tan Y, Sun Z, Meng H et al (2019) Efficient and selective removal of congo red by mesoporous amino-modified MIL-101(Cr) nanoadsorbents. Powder Technol 356:162–169. https://doi.org/10.1016/j.powtec.2019.08.017

Teng H, Hsieh C-T (1999) Activation energy for oxygen chemisorption on carbon at low temperatures. Ind Eng Chem Res 38:292–297. https://doi.org/10.1021/ie980107j

Thomas HC (1944) Heterogeneous ion exchange in a flowing system. J Am Chem Soc 66:1664–1666. https://doi.org/10.1021/ja01238a017

Tong M, Liu D, Yang Q et al (2013) Influence of framework metal ions on the dye capture behavior of MIL-100 (Fe, Cr) MOF type solids. J Mater Chem A 1:8534. https://doi.org/10.1039/c3ta11807j

Vijayaraghavan K, Padmesh T, Palanivelu K, Velan M (2006) Biosorption of nickel(II) ions onto *Sargassum wightii*: application of two-parameter and three-parameter isotherm models. J Hazard Mater 133:304–308. https://doi.org/10.1016/j.jhazmat.2005.10.016

Weber WJ, Morris JC (1963) Kinetics of adsorption on carbon from solution. J Sanit Eng Div 89:31–60

Wu FC, Tseng RL, Juang RS (2009) Initial behavior of intraparticle diffusion model used in the description of adsorption kinetics. Chem Eng J. https://doi.org/10.1016/j.cej.2009.04.042

Wu S, You X, Yang C, Cheng J (2017) Adsorption behavior of methyl orange onto an aluminum-based metal organic framework, MIL-68(Al). Water Sci Technol 75:2800–2810. https://doi.org/10.2166/wst.2017.154

Wu J, Chen K, Tan X et al (2018) Core-shell CMNP@PDAP nanocomposites for simultaneous removal of chromium and arsenic. Chem Eng J 349:481–490. https://doi.org/10.1016/j.cej.2018.05.114

Xu X, Gao B, Tan X et al (2013) Nitrate adsorption by stratified wheat straw resin in lab-scale columns. Chem Eng J 226:1–6. https://doi.org/10.1016/j.cej.2013.04.033

Yagub MT, Sen TK, Afroze S, Ang HM (2014) Dye and its removal from aqueous solution by adsorption: a review. Adv Colloid Interface Sci 209:172–184. https://doi.org/10.1016/j.cis.2014.04.002

Yan G, Viraraghavan T, Chen M (2001) A new model for heavy metal removal in a biosorption column. Adsorpt Sci Technol 19:25–43. https://doi.org/10.1260/0263617011493953

Yao Y, Bing H, Feifei X, Xiaofeng C (2011) Equilibrium and kinetic studies of methyl orange adsorption on multiwalled carbon nanotubes. Chem Eng J 170:82–89. https://doi.org/10.1016/j.cej.2011.03.031

Yoon YH, Nelson JH (1984) Application of gas adsorption kinetics I. A theoretical model for respirator cartridge service life. Am Ind Hyg Assoc J 45:509–516. https://doi.org/10.1080/15298668491400197

Zhang B-L, Qiu W, Wang P-P et al (2020) Mechanism study about the adsorption of Pb(II) and Cd(II) with iron-trimesic metal–organic frameworks. Chem Eng J 385:123507. https://doi.org/10.1016/j.cej.2019.123507

Zheng C, Bennett GD (2002) Applied contaminant transport modeling. Wiley, New York

Zhou X, Zhou X (2014) The unit problem in the thermodynamic calculation of adsorption using the Langmuir equation. Chem Eng Commun 201:1459–1467. https://doi.org/10.1080/00986445.2013.818541

Zhu B-J, Yu X-Y, Jia Y et al (2012) Iron and 1,3,5-benzenetricarboxylic metal–organic coordination polymers prepared by solvothermal method and their application in efficient As(V) removal from aqueous solutions. J Phys Chem C 116:8601–8607. https://doi.org/10.1021/jp212514a

Affiliations

A. Karami[1] · R. Sabouni[1] · M. H. Al-Sayah[2] · A. Aidan[1]

✉ R. Sabouni
rsabouni@aus.edu

[1] Department of Chemical Engineering, American University of Sharjah, Sharjah, United Arab Emirates

[2] Department of Biology, Chemistry and Environmental Sciences, American University of Sharjah, Sharjah, United Arab Emirates